

# Fine-structure collision strengths and line ratios for [Ne v] in infrared and optical sources

Michael Dance,<sup>★</sup> Ethan Palay, Sultana N. Nahar and Anil K. Pradhan<sup>†</sup>

*Department of Astronomy, The Ohio State University, Columbus, OH 43210, USA*

Accepted 2013 July 25. Received 2013 July 24; in original form 2013 March 11

## ABSTRACT

New collisions' strengths for the mid-infrared (mid-IR) and optical transitions in Ne v are presented. Breit–Pauli-R-Matrix calculations for electron impact excitation are carried out with fully resolved near-threshold resonances at very low energies. In particular, the fine-structure lines at 14 and 24  $\mu\text{m}$  due to transitions among the ground state levels  $1s^2 2s^2 2p^3 \ ^3P_{0,1,2}$ , and the optical/near-ultraviolet lines at 2973, 3346 and 3426  $\text{\AA}$  transitions among the  $\ ^3P_{0,1,2}$ ,  $\ ^1D_2$ ,  $\ ^1S_0$  levels are described. Maxwellian-averaged collision strengths are tabulated for all forbidden transitions within the ground configuration. While some significant differences are found for both the far infrared and the optical transitions compared to previous results, computed line emissivity ratios are in good agreement, but change rapidly in the low temperature range  $T_e < 10\ 000\ \text{K}$ . An analysis of the 14/24  $\mu\text{m}$  ratio in low-energy-density (LED) plasma conditions reveals considerable variation; the effective rate coefficient may be dominated by the very low energy behaviour rather than the Maxwellian-averaged collision strengths. Computed values suggest a possible solution to the anomalous mid-IR ratios found to be lower than theoretical limits observed from planetary nebulae and Seyfert galaxies. While such LED conditions may be present in infrared sources, they might be inconsistent with photoionization equilibrium models.

**Key words:** atomic data – atomic processes – ISM: atoms – planetary nebulae: general – photodissociation region (PDR).

## 1 INTRODUCTION

Several ionization stages of carbon-like ions provide useful diagnostics in the mid- to far-infrared (MIR–FIR) space-borne observations as well as prominently observed optical lines from ground-based instruments. Nebular plasmas are generally the most common sources of these lines arising from forbidden transitions within the levels of the ground configuration of C-like ions (viz. Dopita & Sutherland 2003; Pradhan & Nahar 2011). Owing to much lower extinction than optical/ultraviolet lines, the MIR and FIR reveal spatially extended sources to much greater depths. Therefore, in recent years space-based observatories have provided added impetus to the analysis of MIR and FIR lines observed by *Spitzer*, *Herschel* and *Sofia*. In addition to molecular clouds photoionized by hot stars into nebulae, a much wider variety of astronomical objects whose physical conditions may be explored with MIR [Ne v] lines. These range from active galactic nuclei (AGN; Melendez et al. 2011; Perez-Beaupuits, Spoon & Smith 2011; Smith et al. 2012; Stern et al.

2012), metal-rich H II regions (Furness et al. 2010), dusty environments of ultraluminous infrared galaxies (Houck et al. 2004, 2005; Nagao et al. 2011) to blue compact dwarf galaxies (Izotov, Thuan & Privon 2012).

H II regions in general, and planetary nebulae (PNe) in particular, are the testing grounds as well as points of application of forbidden line ratios diagnostics with respect to temperature, density and chemical abundances. The PNe are relatively bright and apparently simple objects that act as astrophysical laboratories to study basic atomic processes. However, several previous studies have discussed problems regarding [Ne v] lines (Clegg et al. 1987; Oliva, Pasquali & Reconditi 1996; van Hoof et al. 2000). Based on the MIR 14/24  $\mu\text{m}$  line ratio, Rubin et al. (2001) and Rubin (2004) pointed out that for a number of PNe, the observed values lie much lower than theoretically possible emissivity ratios at standard nebular temperatures and densities. More recently, in studies of spectral energy distributions in AGN using high-ionization MIR lines, a number of observations also reveal anomalous 14/24  $\mu\text{m}$  line ratios found to be below the theoretical limit (viz. Pereira-Santaella et al. 2010; Tommasin et al. 2010; Weaver et al. 2010; Melendez et al. 2011). Although the line-forming regions in Seyfert galaxies may be dust obscured, the lower than predicted ratios are not countenanced by derived MIR extinction (Li & Draine

<sup>★</sup> Present address: Biomedical Program, University of Toledo, Toledo, OH, USA.

<sup>†</sup> E-mail: pradhan.1@osu.edu

2001). It is important to address this issue in order to use the observed [Ne v] line ratio as density diagnostics, as the emissivity ratios indicate. Moreover, a deviation from theoretical limits of the otherwise clean and uncluttered spectral [Ne v] lines also renders the determination of MIR extinction uncertain (Melendez et al. 2011).

The analysis of the MIR and FIR space observations still rests on our understanding of nebular astrophysics. Forbidden lines are the primary diagnostics for low-temperature and low-density plasmas. In principle, the atomic physics is relatively straightforward: electron impact excitation of low-lying levels followed by radiative decay via magnetic-dipole or electric-quadrupole transitions. These are the only two parameters required for simple collisional-radiative models, usually involving no more than the few levels of the ground configuration. However, it is well known that the electron impact excitation collision strengths and the relevant transition probabilities need to be calculated to high accuracy in order to determine the temperature–density regimes in the source. For example, C-like ground configuration  $1s^2 2s^2 2p^3$  gives rise to three LS terms and five fine-structure levels  $^3P_{0,1,2}$ ,  $^1D_2$ ,  $^1S_0$ . In an earlier study, Palay et al. (2012) showed that near-threshold resonances in the collision strengths of C-like [O III] make significant contribution to fine-structure transitions. Rather elaborate computations including relativistic and resonance effects are necessary in order to delineate resonances and obtain accurate rate coefficients. In this work, we study the transitions in the Ne v ion and find similar effects. As Rubin et al. (2001) and Rubin (2004) have noted, different sets of collision strength data available in literature (viz. Lennon & Burke 1991, 1994; Griffin & Badnell 2000) did not resolve the discrepancy in the 14/24 ratio lying below the theoretical low density limit. The aim of this paper is to re-examine the Ne v collision strengths and line ratios computed using the Breit–Pauli-R-Matrix (BPRM) method (Berrington, Eissner & Norrington 1995), with particular emphasis on the MIR lines under low-energy-density (LED) conditions. These conditions are likely to exist only in plasmas that are not in photoionization equilibrium, but probably lie at the interface of warm and cold nebular gas. As we show in this paper, a comparison of the computed line emissivity ratios with observations of a number of PNe points to much lower than equilibrium temperatures. In order to examine the theoretical behaviour, we also extend the calculations to  $T_e < 1000$  K, not considered in previous works. Based on the more accurate data computed herein, the results should enable revised interpretation of MIR [Ne v] lines and originating plasma environments.

## 2 THEORY AND COMPUTATIONS

A brief theoretical description of the BPRM calculations is as follows (a discussion of the general methodology and application to atomic processes is given, for example, in Pradhan & Nahar 2011).

### 2.1 The Breit–Pauli approximation

The relativistic BPRM Hamiltonian is given as

$$H_{N+1}^{\text{BP}} = \sum_{i=1}^{N+1} \left\{ -\nabla_i^2 - \frac{2Z}{r_i} + \sum_{j>i}^{N+1} \frac{2}{r_{ij}} \right\} + H_{N+1}^{\text{mass}} + H_{N+1}^{\text{Dar}} + H_{N+1}^{\text{so}}, \quad (1)$$

where the last three terms are relativistic corrections, respectively:

$$\text{the mass correction term, } H^{\text{mass}} = -\frac{\alpha^2}{4} \sum_i p_i^4,$$

$$\text{the Darwin term, } H^{\text{Dar}} = \frac{Z\alpha^2}{4} \sum_i \nabla^2 \left( \frac{1}{r_i} \right),$$

$$\text{the spin–orbit interaction term, } H^{\text{so}} = Z\alpha^2 \sum_i \frac{1}{r_i^3} l_i \cdot s_i. \quad (2)$$

Equation (2) represents the one-body terms of the Breit interaction. In addition, another version of BPRM codes including the two-body terms of the Breit–interaction (Pradhan & Nahar 2011; Nahar et al. 2003; Eissner & Chen, in preparation) has been developed and is employed in this work.

### 2.2 Ne v target representation

The coupled channel method embodied in the BPRM approximation is crucially dependent on the accuracy of the wavefunctions of the  $N$ -electron target ion included to represent the  $(N+1)$ -electron ( $e + \text{ion}$ ) system. We employ the general purpose atomic structure code SUPERSTRUCTURE (Eissner, Jones & Nussbaumer 1974) to compute a wavefunction expansion including the first 20 fine-structure levels. Table 1 compares the calculated eigenenergies with experimental values tabulated by the US National Institute of Standards and Technology ([www.nist.gov](http://www.nist.gov)).

The spectroscopic levels and configurations included in the ( $e + \text{Ne v}$ ) wavefunction expansion are as in Table 1. The full configuration–interaction basis set optimized with SUPERSTRUCTURE is (Eissner et al. 1974; Nahar et al. 2011)

$$\begin{aligned} & [1s^2]2s^2 2p^2, 2s 2p^3, 2s^2 2p 3s, 2p^4, 2s^2 2p 3p, 2s^2 2p 3d, \\ & 2s^2 2p 4s, 2s^2 2p 4p, 2s 2p^2 3s, \\ & 2s 2p^2 3p, 2s 2p^2 3d, 2s^2 3s^2, 2s^2 3p^2, 2s^2 3d^2, 2s^2 4s^2, 2s^2 4p^2, \\ & 2s^2 3s 3p, 2s^2 3s 3d, 2s^2 3s 4s, 2s^2 3s 4p, 2s^2 3p 3d, 2p^3 3s, 2p^3 3p, 2p^3 3d. \end{aligned}$$

**Table 1.** Levels and energies ( $E_t$ ) of target (core ion) Ne v.

| Level | $J_t$                 | $E_t$ (Ry) |           |
|-------|-----------------------|------------|-----------|
|       |                       | NIST       | SS        |
| 1     | $1s^2 2s^2 2p^2(^3P)$ | 0          | 0.0       |
| 2     | $1s^2 2s^2 2p^2(^3P)$ | 1          | 0.003 758 |
| 3     | $1s^2 2s^2 2p^2(^3P)$ | 2          | 0.010 116 |
| 4     | $1s^2 2s^2 2p^2(^1D)$ | 2          | 0.276 036 |
| 5     | $1s^2 2s^2 2p^2(^1S)$ | 2          | 0.582 424 |
| 6     | $1s^2 2s 2p^3(^5S^o)$ | 2          | 0.8052    |
| 7     | $1s^2 2s 2p^3(^3D^o)$ | 3          | 1.602 32  |
| 8     | $1s^2 2s 2p^3(^3D^o)$ | 2          | 1.602 96  |
| 9     | $1s^2 2s 2p^3(^3D^o)$ | 1          | 1.603 16  |
| 10    | $1s^2 2s 2p^3(^3P^o)$ | 2          | 1.896 87  |
| 11    | $1s^2 2s 2p^3(^3P^o)$ | 1          | 1.896 87  |
| 12    | $1s^2 2s 2p^3(^3P^o)$ | 0          | 1.897 19  |
| 13    | $1s^2 2s 2p^3(^1D^o)$ | 2          | 2.465 56  |
| 14    | $1s^2 2s 2p^3(^3S^o)$ | 1          | 2.545 76  |
| 15    | $1s^2 2s 2p^3(^1P^o)$ | 1          | 2.768 54  |
| 16    | $1s^2 2p^4(^3P)$      | 2          | 3.760 63  |
| 17    | $1s^2 2p^4(^3P)$      | 1          | 3.767 78  |
| 18    | $1s^2 2p^4(^3P)$      | 0          | 3.770 85  |
| 19    | $1s^2 2p^4(^1D)$      | 2          | 4.138 16  |
| 20    | $1s^2 2p^4(^1S)$      | 0          | 4.744 72  |

**Table 2.** Effective Maxwellian-averaged collision strengths.

| Transition    | $\lambda$           | $\Upsilon(100)$ | $\Upsilon(500)$ | $\Upsilon(1000)$ | $\Upsilon(5000)$ | $\Upsilon(10\ 000)$ | $\Upsilon(20\ 000)$ | $\Upsilon(30\ 000)$ |
|---------------|---------------------|-----------------|-----------------|------------------|------------------|---------------------|---------------------|---------------------|
| $^3P_0-^3P_1$ | 24 $\mu\text{m}$    | 2.72(0)         | 3.02(0)         | 2.78(0)          | 2.09(0)          | 1.69(0)             | 1.28(0)             | 1.07(0)             |
| $^3P_2-^3P_0$ | 9 $\mu\text{m}$     | 2.70(0)         | 3.00(0)         | 3.16(0)          | 2.56(0)          | 1.93(0)             | 1.34(0)             | 1.04(0)             |
| $^3P_2-^3P_1$ | 14 $\mu\text{m}$    | 8.48(0)         | 9.18(0)         | 9.55(0)          | 8.02(0)          | 6.26(0)             | 4.49(0)             | 3.60(0)             |
| $^1D_2-^3P_0$ | 3301.3 $\text{\AA}$ | 1.23(-1)        | 1.20(-1)        | 1.22(-1)         | 1.80(-1)         | 1.95(-1)            | 2.09(-1)            | 2.19(-1)            |
| $^1D_2-^3P_1$ | 3345.8 $\text{\AA}$ | 3.76(-1)        | 3.67(-1)        | 3.69(-1)         | 5.37(-1)         | 5.84(-1)            | 6.27(-1)            | 6.58(-1)            |
| $^1D_2-^3P_2$ | 3425.9 $\text{\AA}$ | 6.61(-1)        | 6.46(-1)        | 6.47(-1)         | 9.22(-1)         | 9.97(-1)            | 1.07(0)             | 1.1(0)              |
| $^1S_0-^3P_0$ | –                   | 4.60(-2)        | 4.82(-2)        | 4.84(-2)         | 3.58(-2)         | 3.15(-2)            | 2.98(-2)            | 2.94(-2)            |
| $^1S_0-^3P_1$ | 1574.8 $\text{\AA}$ | 1.35(-1)        | 1.42(-1)        | 1.42(-1)         | 1.04(-1)         | 9.13(-2)            | 8.73(-2)            | 8.69(-2)            |
| $^1S_0-^3P_2$ | 1592.3 $\text{\AA}$ | 2.24(-1)        | 2.35(-1)        | 2.35(-1)         | 1.73(-1)         | 1.53(-1)            | 1.47(-1)            | 1.45(-1)            |
| $^1S_0-^1D_2$ | 2972.8 $\text{\AA}$ | 3.51(-1)        | 4.51(-1)        | 4.88(-1)         | 6.69(-1)         | 6.26(-1)            | 6.33(-1)            | 6.87(-1)            |

The optimized scaling parameters in the Thomas–Fermi–Dirac potential are 1.476 37, 1.476 37, 1.271 84, 1.476 37, 1.271 84, 1.193 06, 1.476 37 and 1.271 84 for the 1s, 2s, 2p, 3s, 3p, 3d, 4s and 4p, orbitals, respectively. Although the computed energies are generally within a few per cent of the observed values, the latter are used in the BPRM calculations to ensure precise resonance positions relative to the Ne v target thresholds. The collision strengths were computed employing the extended BPRM codes including a full representation of the two-body Breit terms (Eissner & Chen, in preparation). It is important to ensure convergence of collision strengths with respect to partial waves and energy resolution. Total (e + ion) symmetries up to (LS)J $\pi$  with  $J \leq 19.5$  were included in the calculations, though it was found that the collision strengths for all forbidden-transition transitions converged for  $J \leq 9.5$ . A very fine energy mesh of  $\Delta E < 10^{-6}$  Rydbergs was used to resolve the near-threshold resonances.

### 2.3 Effective collision strengths

The effective collision strengths or rate coefficients are computed by convolving the collision strengths over a Maxwellian function at a given electron temperature  $T_e$  as

$$\Upsilon_{ij}(T_e) = \int_0^\infty \Omega_{ij}(\epsilon) \exp(-\epsilon/kT_e) d(\epsilon/kT_e), \quad (3)$$

where  $E_{ij}$  is the energy difference and  $\Omega_{ij}$  is the collision strength for the transition  $i \rightarrow j$ . Later, we discuss LED plasma conditions where the effective collision strength may differ from the form in equation (3). The excitation rate coefficient is related to the effective collision strength as

$$q_{ij}(T_e) = \frac{8.63 \times 10^{-6}}{g_i T_e^{1/2}} e^{-E_{ij}/kT_e} \Upsilon_{ij}(T_e), \quad (4)$$

where  $g_i$  is the statistical weight of the initial level.

## 3 RESULTS AND DISCUSSION

Collision strengths and line ratios are presented in this section. A discussion of possible implications for LED plasmas in general, and PNe in particular, is also given.

### 3.1 Ground-state fine-structure collision strengths

One of the main aims of the present calculations was complete resolution of resonance structures in near-threshold collision strengths. Fig. 1 shows the resolved Rydberg series of resonances in  $\Omega(^3P_0-^3P_1)$  converging on to the higher  $^3P_2, ^1D_2, ^1S_0$  levels.

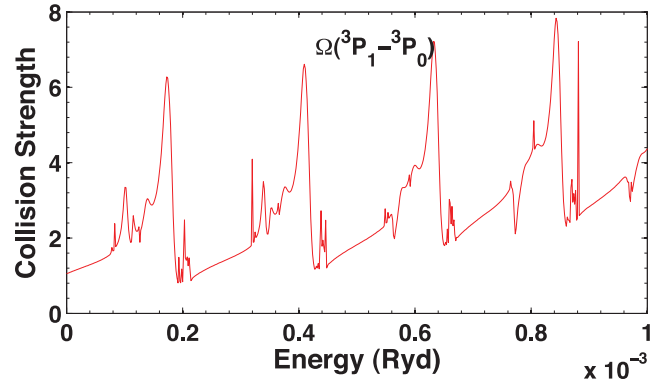


**Figure 1.** Rydberg series of near-threshold resonances in the collision strength for the fine-structure transition  $2p^2(^3P_0-^3P_1)$  corresponding to the 24  $\mu\text{m}$  FIR line. A fine mesh of the order of  $10^{-6}$  Ryd was used to fully resolve the ( $^3P_2, ^1D_2, ^1S_0$ ) $n\ell$  resonances, necessary for accurate rate coefficients at low temperatures.

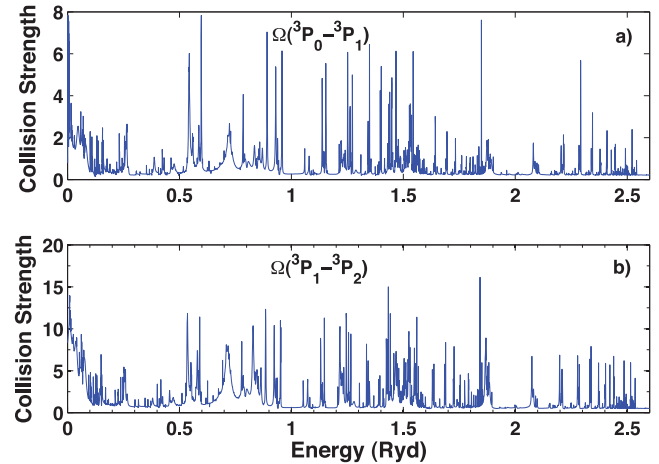


**Figure 2.** Collision strengths over extended energy ranges for fine-structure transitions  $2p^2(^3P_0-^3P_1, ^3P_1-^3P_2)$  at (a) 24  $\mu\text{m}$  and (b) 14  $\mu\text{m}$ , respectively.

The calculations were carried out at an energy interval of  $10^{-6}$  Ryd. These resonances dominate the low-energy-temperature behaviour of the detailed as well as the averaged, collision strengths. The corresponding 24  $\mu\text{m}$  line is the one most affected. Fig. 2 shows the results over an extended energy range for  $\Omega(^3P_0-^3P_1)$  and  $\Omega(^3P_1-^3P_2)$ . Particularly noteworthy is the significant rise close to thresholds for both transitions.

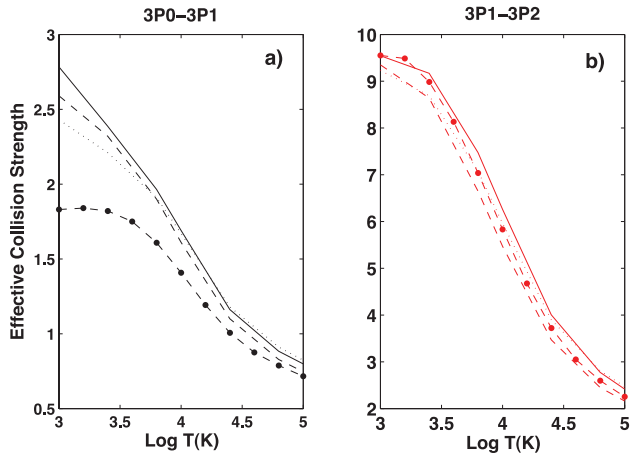


**Figure 3.** Maxwellian-averaged effective collision strengths  $\Upsilon(T_e)$  for the transitions  $2p^2(^3P_0-^3P_1, ^3P_1-^3P_2)$  at (a)  $24\ \mu\text{m}$  and (b)  $14\ \mu\text{m}$  (cf. Fig. 2): solid line. The dot-dashed lines show previous results without relativistic effects (Lennon & Burke 1994); the dotted and dashed lines show 20-level BPRM and 138-level ICFT results, respectively (Griffin & Badnell 2000), available in the temperature range  $T_e > 1000\ \text{K}$ .

The Maxwellian-averaged collision strengths are plotted in Fig. 3 (solid curve), and compared with previous results from Lennon & Burke (1994; dot-dashed curve) and two sets of calculations by Griffin & Badnell (2000). The latter work employed two different approximations, a 20-level BPRM calculation (dotted curve) and a more extensive intermediate-coupling fine-structure transformation (ICFT, dashed curve). The ICFT approach is based on the method introduced by Eissner et al. (1974), whereby the LS coupling collisional reactance matrices are algebraically recoupled to an LSJ scheme and transformed via term-coupling coefficients obtained on diagonalizing the target  $N$ -electron Breit–Pauli Hamiltonian, as essentially incorporated in the code *SUPERSTRUCTURE*. The Eissner et al. method has been widely employed to take limited account of relativistic effects in otherwise non-relativistic LS coupling calculations and has been employed in codes such as *JAJOM* (Saraph 1972, 1978) and *STGFJ* (e.g. Luo & Pradhan 1990). In addition, the ICFT method employs multichannel quantum defect theory in the intermediate coupling transformation of the full reactance matrix including weakly coupled closed channels, and it is a closer approximation to BPRM particularly for high- $n$  Rydberg resonances below threshold(s). For the  $24\ \mu\text{m}$  transition, we find differences of up to 14 per cent at the lowest temperatures with the otherwise similar previous 20-level BPRM results, most likely attributable to improved resolution at very low energies in the present calculations. Differences no larger than 10 per cent are found for the  $14\ \mu\text{m}$  transition between all sets of calculations.

The present calculations are also carried out at  $T_e < 1000\ \text{K}$ , not considered in previous works. Since we have taken particular care to fully resolve the near-threshold collision strengths, the effective collision strengths should be limited only by the intrinsic accuracy of the BPRM calculations and not by numerical resolution of resonances. That is necessary in order to interpret the line ratio observations in cases where they do not fall in the nebular temperature range, as discussed next.

### 3.2 The $14/24\ \mu\text{m}$ emissivity ratio and observations

Owing to small differences in excitation energies, the fine-structure line ratios due to transitions within the ground state levels  $^3P_{0,1,2}$

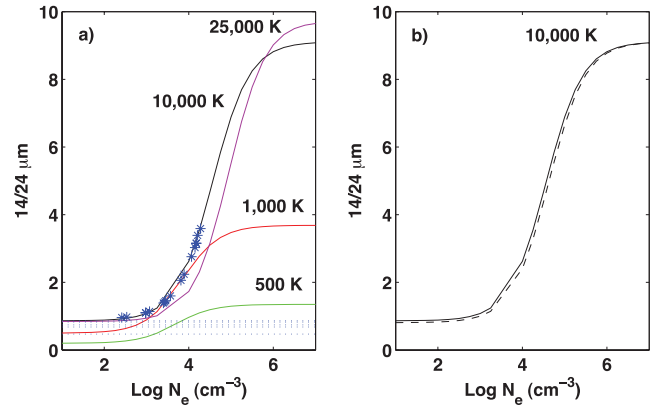


**Figure 4.** The density and temperature dependence of the  $14/24\ \mu\text{m}$  line emissivity ratios. (a) The solid lines represent line ratios at four temperatures. Asterisks denote observed line ratios from PNe (Rubin 2004), at  $T_e = 10\ 000\ \text{K}$  with assigned densities. The dotted lines represent observed line ratios that are out of range of typical nebular temperature–density range (Rubin 2004), except at much lower temperatures. (b) The solid curves represent the present results and the dashed lines represent the results obtained using the Griffin & Badnell (2000) collision strengths; Lennon & Burke (1994) data yield the same results. Large differences in line ratios are not found because of *systematic* differences of similar magnitude for both lines between previous and present rate coefficients.

are not highly temperature sensitive in the typical nebular range around  $10\ 000\ \text{K}$ . On the other hand, this emissivity ratio is highly density sensitive at typical nebular densities of  $10^{3-6}\ \text{cm}^{-3}$ . Rubin (2004) has tabulated the  $14/24$  line flux ratio from a number of PNe and noted that it falls *below* the theoretically possible value of approximately 1.0 in about half the observations. Fig. 4 shows the measured line ratios; the asterisks denote the derived densities for the PNe that fall very well on the  $10\ 000\ \text{K}$  emissivity ratio curve. However, the observed values from some of the anomalous PNe are seen as lying around the emissivity ratio curve at  $1000\ \text{K}$  or lower, shown as vertical dashed band in Fig. 4. One can readily find low-temperature curves versus density that could account for these ratios lying below the  $10\ 000\ \text{K}$  curve. Incidentally, variations by similar amounts in both transitions yield very good agreement with ratios at  $T_e > 10\ 000\ \text{K}$  with previous works shown in the right-hand panel; both the Lennon & Burke (1994) and Griffin & Badnell (2000) data yield indistinguishable results.

The present calculations employ a basis set of configurations designed to focus on very low lying levels. The omission of higher odd-parity states than in Table 1 might affect the dipole polarizability of the three lowest even parity terms, and hence the low-energy scattering cross-sections. However, based on this work, we can rule out further uncertainties in the collision strengths. Fig. 4 illustrates the dichotomy between the PNe with normal density sensitivity of the  $14/24$  ratio and a fair number of those that appear to correspond to much lower temperatures than that which characterizes typical nebular photoionization equilibrium. While the equilibrium models may not explain these values, it is worth examining the behaviour of line ratios in LED plasmas in general. Equation (3) implies that

$$\lim_{T \rightarrow 0} \Upsilon(T) = \lim_{E \rightarrow 0} \Omega(E). \quad (5)$$

Between  $1000$  and  $10\ 000\ \text{K}$ , the Maxwellian factor involves exponential factor  $\exp(-E/kT_e)$  ranging from  $\exp(-158E)$  to  $\exp(-15.8E)$  in Rydberg units. Therefore,  $\Upsilon(T)$  depends entirely on the detailed behaviour of  $\Omega(E)$ . Furthermore, if we also consider the fact that low densities  $N_e \approx 10^2\ \text{cm}^{-3}$  may exist, a departure

from the normal Maxwellian distribution under LED conditions is possible. Therefore, the rate coefficient would tend to follow the collision strengths *and* variations with resonance structures at very low energies close to excitation threshold(s). This suggestion is offered to re-examine non-equilibrium conditions that might prevail in LED plasma sources, which may also not have established a Maxwellian distribution. The emitted line intensity would then depend on the actual kinetic energy and number density of electrons at a given energy. In addition, the electron and ion temperatures may differ, i.e.  $T_e \neq T_i$ .

### 3.3 [Ne v] optical collision strengths and line ratios

Collision strengths for forbidden optical transitions within ground configuration levels are shown in Fig. 5:  $^3P_1-^1D_2$ ,  $^3P_2-^1D_2$  and  $^1S_0-^1D_2$  at  $\lambda\lambda$  3345.8, 3425.9 and 2972.8, respectively. Resonance structures due to Ne v target excitation thresholds given in Table 1 manifest themselves at all energies and need to be considered in the calculation of averaged collision strengths. Whereas the agreement with previous works (Lennon & Burke 1994; Griffin & Badnell 2000) is found to be satisfactory, generally 10–15 per cent or better, for some of the relatively weak transitions there are marked differences. Fig. 6 compares the present results for the Maxwellian-averaged collision strengths for two transitions,  $^3P_0-^1D_2$  and  $^3P_0-^1S_0$ , that do not directly correspond to observed lines but enter in the solution of rate equations for line emissivities.

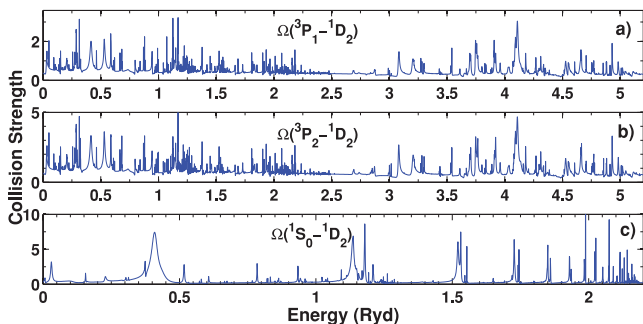


**Figure 5.** Collision strengths for the forbidden optical transitions  $2p^2(^3P_1-^1D_2)$ ,  $^3P_2-^1D_2$  and  $^1S_0-^1D_2$  at 3346, 3426 and 2973 Å, respectively.

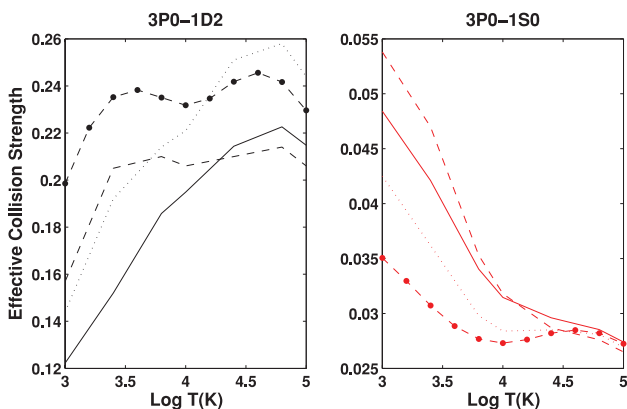


**Figure 6.** Maxwellian-averaged collision strengths  $\Upsilon(T_e)$  for the transitions  $2p^2(^3P_0-^1D_2)$ ,  $^3P_0-^1S_0$ : solid lines. The dash-dotted lines show previous results without relativistic effects (Lennon & Burke 1994); dotted and dashed lines show 20-level BPRM and 138-level ICFT results, respectively (Griffin & Badnell 2000).

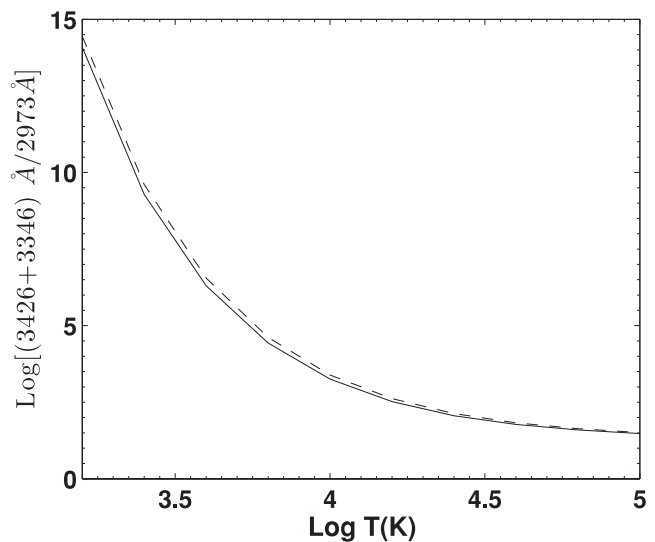


**Figure 7.** Blended [Ne v] optical line ratio  $(3346+3426)/2973$  versus  $T_e$  at  $N_e = 10^3 \text{ cm}^{-3}$ . Despite significant differences in the collision strengths, the optical emissivity ratios agree with those using earlier data by Lennon & Burke (1994) owing to systematic enhancements in the same direction.

The differences are found to be rather large, 16 per cent for  $^3P_0-^1D_2$  and 20 per cent for the  $^3P_0-^1D_2$  transitions. Nevertheless, the important optical line ratios are not significantly affected, as shown in Fig. 7. The blended emissivity ratio  $(3426+3346)/2973$  differs little from those derived from earlier values from Lennon & Burke (1994).

### 3.4 Maxwellian-averaged collision strengths

In Table 2, we present the effective collision strengths (equation 3) for the 10 transitions among the ground configuration levels and their wavelengths. The tabulation is carried out at a range of temperatures typical of nebular environments, including the low-temperature range  $T \leq 1000 \text{ K}$  not heretofore considered.

## 4 CONCLUSION

New calculations for [Ne v] collision strengths are reported including relativistic and resonance effects at very low energies that affect the low temperature rate coefficients not heretofore calculated. In particular, a precise delineation of near-threshold resonance structures has a significant effect on the MIR 14/24  $\mu\text{m}$  line emissivities. However, low-density theoretical limits of the ratios computed at typical nebular temperatures  $T_e \approx 10\,000 \text{ K}$  are still higher than the anomalously low values of observations from a number of PNe discussed by Rubin et al. (2001) and Rubin (2004). Since the Maxwellian-averaged collision strengths generally decrease with temperature, and simulate the behaviour of collision strengths at low energies, it is suggested that non-equilibrium conditions corresponding to LED plasma conditions might possibly account for the low observed 14/24 ratios. In any case, the low temperature rate coefficients for  $T_e < 10\,000 \text{ K}$  are likely to be uncertain owing to resonances.

The [Ne v] forbidden optical collision strengths are generally in good agreement with previous works, and the prominent line ratios are not much influenced. Finally, as noted in the previous work on [O III] lines (Palay et al. 2012), for higher temperatures  $T > 20\,000 \text{ K}$  proton impact excitation of the ground-state fine-structure levels

$^3P_{0,1,2}$  needs to be taken into account; at lower temperatures the excitation rate coefficient due to electrons far exceeds that due to protons (Ryans et al. 1999).

The main conclusions are as follows. (i) More detailed BPRM calculations confirm the overall accuracy of previous results, and line emissivities at typical nebular temperatures  $T_e \geq 10\,000$  K are not much effected. (ii) Low temperature rate coefficients vary rapidly and are highly susceptible to near-threshold resonances. (iii) The 14/24  $\mu\text{m}$  emissivity ratios at  $T_e \approx 1000$  K yield values that do encompass the anomalously low observed line ratios. (iv) A possible explanation of discrepancies found in astronomical observations of the 14/24  $\mu\text{m}$  line ratio lies not so much in the accuracy of the atomic rates, but in astrophysical scenarios that might countenance non-equilibrium LED conditions.

Collision strengths for all 190 transitions among energy levels in Table 1 may be obtained from Ethan Palay (palay.5@buckeyemail.osu.edu) or the NORAD Atomic Database compiled by S. N. Nahar (www.astronomy.ohio-state/~nahar).

## ACKNOWLEDGEMENTS

We are grateful to Robert Rubin (deceased) for suggesting this study and communications. The computational work was carried out at the Ohio Supercomputer Center in Columbus Ohio. This work was partially supported by a grant from the NASA Astrophysical Research and Analysis programme. EP would like to gratefully acknowledge a Summer Undergraduate Research Program grant from the Ohio State University.

## REFERENCES

- Berrington K. A., Eissner W., Norrington P. H., 1995, *Comput. Phys. Commun.*, 92, 290
- Clegg R. E. S., Harrington J. P., Barlow M. J., Walsh J. R., 1987, *ApJ*, 314, 551
- Dopita M. A., Sutherland R. S., 2003, *Astrophysics of the Diffuse Universe*. Springer-Verlag, Berlin
- Eissner W., Jones M., Nussbaumer H., 1974, *Comput. Phys. Commun.*, 8, 270
- Furness J. P., Crowther P. A., Morris P. W., Barbosa C. L., Blum R. D., Conti P. S., van Dyk S. D., 2010, *MNRAS*, 403, 1433
- Griffin D., Badnell N. R., 2000, *J. Phys. B*, 33, 4389
- Houck J. R. et al., 2004, *ApJS*, 154, 18
- Houck J. R. et al., 2005, *ApJ*, 622, L105
- Izotov Y. I., Thuan T. X., Privon G., 2012, *MNRAS*, 427, 1299
- Lennon D. J., Burke V. M., 1991, *MNRAS*, 251, 628
- Lennon D. J., Burke V. M., 1994, *A&AS*, 103, 273
- Li A., Draine B. T., 2001, *ApJ*, 554, 778
- Luo D., Pradhan A. K., 1990, *Phys. Rev. A*, 41, 165
- Melendez M., Kraemer S. B., Weaver K. A., Mushotzky R. F., 2011, *ApJ*, 738, 6
- Nagao T., Maiolino R., Marconi A., Matsuhara H., 2011, *A&A*, 526, A149
- Nahar S. N., Eissner W., Chen G.-X., Pradhan A. K., 2003, *A&A*, 408, 789
- Nahar S. N., Pradhan A. K., Montenegro M., Eissner W., 2011, *Phys. Rev. A*, 83, 053417
- Oliva E., Pasquali A., Reconditi M., 1996, *A&A*, 305, L21
- Palay E., Nahar S. N., Pradhan A. K., Eissner W., 2012, *MNRAS*, 423, L35
- Pereira-Santaella M., Diamond-Stanic A. M., Alonso-Herrero A., Rieke G. H., 2010, *ApJ*, 725, 2270
- Perez-Beaupuits J. P., Spoon H. W. W., Smith J. D., 2011, *A&A*, 536, 56
- Pradhan A. K., Nahar S. N., 2011, *Atomic Astrophysics and Spectroscopy*. Cambridge Univ. Press, Cambridge
- Rubin R. H., 2004, in Duc P.-A., Braine J., Brinks E., eds, *Proc. IAU Symp.* 217, *Recycling Intergalactic and Interstellar Matter*. Astron. Soc. Pac., San Francisco, p. 190
- Rubin R. H., Dufour R. J., Geballe T. R., Colgan S. W. J., Harrington J. P., Lord S. D., Liao A. L., Levine D. A., 2001, in Ferland G., Savin W. D., eds, *ASP Conf. Ser. Vol. 247, Spectroscopic Challenges of Photoionized Plasmas*. Astron. Soc. Pac., San Francisco, p. 479
- Ryans R. S. I., Foster-Woods V. J., Reid R. H. G., Keenan F. P., 1999, *A&A*, 345, 663
- Saraph H. E., 1972, *Comput. Phys. Commun.*, 3, 256
- Saraph H. E., 1978, *Comput. Phys. Commun.*, 15, 247
- Smith K. L., Shields G. A., Stevens A. C., Rosario D. J., 2012, *ApJ*, 752, 63
- Stern D. et al., 2012, *ApJ*, 753, 30
- Tommasin S., Spinioglio L., Malkan M. A., Fazio G., 2010, *ApJ*, 709, 1257
- van Hoof P. A. M., Beintema D. A., Verner D. A., Ferland G. J., 2000, *A&A*, 354, L41
- Weaver K. A. et al., 2010, *ApJ*, 716, 1151

This paper has been typeset from a  $\text{\TeX}/\text{\LaTeX}$  file prepared by the author.